# Efficiency Enhanced Hybrid Solar Cells Using a Blend of Quantum Dots and Nanorods

*Krischan F. Jeltsch, Martin Schädel, Jörg-Bernd Bonekamp, Phenwisa Niyamakom, Frank Rauscher, Hans W. A. Lademann, Ines Dumsch, Sybille Allard, Ullrich Scherf, and Klaus Meerholz**

**The cell performance of organic-inorganic hybrid photovoltaic devices based on CdSe nanocrystals and the semiconducting polymer poly[2,6-(4,4-bis(2-ethylhexyl)-*4H*-cyclopenta[2,1-*b*;3,4-*b*']-dithiophene)-*alt*-4,7-(2,1,3-benzothiadiazole)] (PCPDTBT) is strongly dependent on the applied polymer-to-nanocrystal loading ratio and the annealing temperature. It is shown here that higher temperatures for the thermal annealing step have a beneficial impact on the nanocrystal phase by forming extended agglomerates necessary for electron percolation to enhance the short-circuit current. However, there is a concomitant reduction of the open-circuit voltage, which arises from energy-level alterations of the organic and the inorganic component. Based on quantum dots and PCPDTBT, we present an optimized organic–inorganic hybrid system utilizing an annealing temperature of 210 °C, which provides a maximum power conversion efficiency of 2.8%. Further improvement is obtained by blending nanocrystals of two different shapes to compose a favorable n-type network. The blend of spherical quantum dots and elongated nanorods results in a well-interconnected pathway for electrons within the p-type polmer matrix, yielding maximum efficiencies of 3.6% under simulated AM 1.5 illumination.**

## 1. Introduction

Organic–inorganic hybrid photovoltaics (PV) have attracted increased attention,[1–3] owing to the ease of processibility from solution and the potential for making low-cost solar cells with reasonable stability. Similar to the commercially upcoming bulk-heterojunction (BHJ) organic solar cell technology, which utilizes a purely organic photoactive blend of a semiconducting polymer and a fullerene derivative, hybrid PV takes advantage of increased light harvesting relative to traditional layered heterojunctions, due to the extended interface between the electron-conducting and the hole-conducting component afforded by nanoscale phase separation.[4] Organic–inorganic hybrid PV presents an advantage relative to its all organic counterpart due to the size dependent and thus, adjustable absorption properties of the inorganic, nanostructured materials,[5] which are disadvantageous in the case of widely used phenyl-$C_{61}$-butyric-acid-methyl ester ($PC_{61}BM$) in organic PV cells.[6] Since the first report on a PV cell comprising a blend of a hole conducting polymer poly[2-methoxy-5-(2′-ethylhexyloxy)-*p*-phenylene vinylene] (MEH-PPV) and electron-conducting spherical CdSe nanocrystals (NC) (power conversion efficiency (PCE) = 0.2%, AM = 1.5, 0.5 mW $cm^{-2}$) in 1996,[1] significant improvement of the device efficiency has been achieved. Like for all BHJ-devices, the 3-dimensional nano-morphology is crucial for the device performance. For example, it was demonstrated that the use of larger particles yielded higher currents due to the reduced number of hopping events necessary to cover a certain distance.[7] Similarly, the application of more complex NC structures such as tetrapods resulted in better performing devices through more efficient electron-transport.[8] In both cases, better connected n-type pathways significantly influence the device performance by reducing the particle–particle electrical resistance, originating from surface-bound ligands, which are necessary to stabilize the nanocrystals for suitable processing from suspension. At present, hybrid photovoltaics using a blend of regioregular poly(3-hexylthiophene-2,5-diyl) (P3HT) as a long-time referred absorber material and CdSe NC in the form of quantum dots (0D),[9] nanorods (1D),[10] tetrapods,[11] and hyperbranched (3D)[12] NC exhibit maximum PCE of 2.0%, 2.6%, 2.8%, and 2.2%, respectively.

Similar to fullerene-based cells, the use of the low-band-gap polymer poly[2,6-(4,4-bis(2-ethylhexyl)-4*H*-cyclopenta[2,1-*b*;3,4-*b*']dithiophene)-*alt*-4,7-(2,1,3-benzothiadiazole)] (PCPDTBT) in combination with CdSe tetrapods enhanced the cell performance

K. F. Jeltsch, M. Schädel, H. W. A. Lademann, Prof. K. Meerholz
Department für Chemie
Universität Köln
Luxemburger Straße 116, 50939 Köln, Germany
E-mail: klaus.meerholz@uni-koeln.de
M. Schädel
Q-Cells SE, OT Thalheim, Sonnenallee 17-21,
06766 Bitterfeld-Wolfen, Germany
Dr. J.-B. Bonekamp
Soluxx GmbH, Greinstraße 4, 50939 Köln, Germany
Dr. P. Niyamakom, Dr. F. Rauscher
Bayer Technology Services GmbH
Process Technology
Building E41, 51368 Leverkusen, Germany
I. Dumsch, Dr. S. Allard, Prof. U. Scherf
Institut für Polymertechnologie
Bergische Universität Wuppertal
Gauss-Strasse 20, 42097 Wuppertal, Germany

**DOI: 10.1002/adfm.201101809**

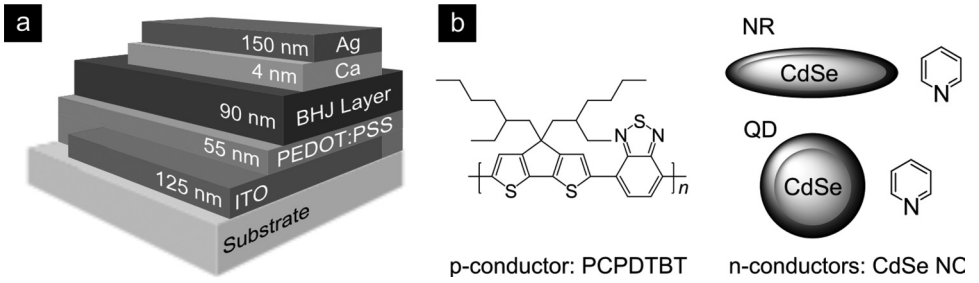


**Figure 1.** a) Schematic setup of the BHJ solar cells. b) Chemical structure and schematic image of the applied materials in the photoactive blend.

and led to the current world-record efficiency in hybrid PV of 3.1%.[13] The advantages of PCPDTBT over P3HT are obvious: The lower bandgap ($E_g$ (PCPDTBT) = 1.5 eV[14], $E_g$ (P3HT) = 2.0 eV[15]), a higher hole mobility ($\mu_h$ (PCPDTBT) = $10^{-2}$ cm$^2$ V$^{-1}$ s$^{-1}$[16], $\mu_h$ (P3HT) = $10^{-5}$–$10^{-4}$ cm$^2$ V$^{-1}$ s$^{-1}$[17]) and an energetically lower lying HOMO (highest occupied molecular orbital) ($E_{HOMO}$ (PCPDTBT) = –5.3eV[16], $E_{HOMO}$ (P3HT) = –4.8eV[15]) clearly satisfy the needs for better performing photovoltaic devices. In this study, PCPDTBT and pyridine capped CdSe NC of two different geometries, spherical quantum dots (QD) and elongated nanorods (NR), were blended together to form BHJ-layers for hybrid solar cells.

## 2. Results and Discussion

### 2.1. Devices based on PCPDTBT and Quantum Dots

The device architecture of the investigated solution-processed solar cells, the chemical structure of PCPDTBT (donor), and schematic illustrations of the two NC shapes used here (QD and NR; acceptor) are presented in **Figure 1**. For device optimization, we studied the donor-to-acceptor ratio (D/A), the active layer thickness *L*, and further investigated the impact of the annealing temperature.

First, we investigated devices containing spherical QDs. The dependence of the device efficiency on the annealing temperature is shown in **Figure 2**a for four different QD contents. It depends strongly on both parameters, which is mostly a result of large changes of the short-circuit current density ($J_{SC}$) (Figure 2b), while the open-circuit voltage ($V_{OC}$) and the fill factor (*FF*) show much less variations (Figure 2c).

Regarding dependence of the device performance on the the D/A ratio, the best performance is achieved for 90 wt% QD loading (squares). There are two counteracting effects to consider. A lower QD content in the blend enhances the number of absorbed photons since the absorption of PCPDTBT is dominant over the QD. Conversely, the transport of photo-generated charges through the active layer is limited at lower QD content due to limited percolation pathways for electrons in the QD network. The relatively high amount of QD (90 wt%) for the best performing devices is thus related to increased electron extraction.

Regarding the annealing temperature, again two regimes can be distinguished. In the lower temperature regime, $J_{SC}$

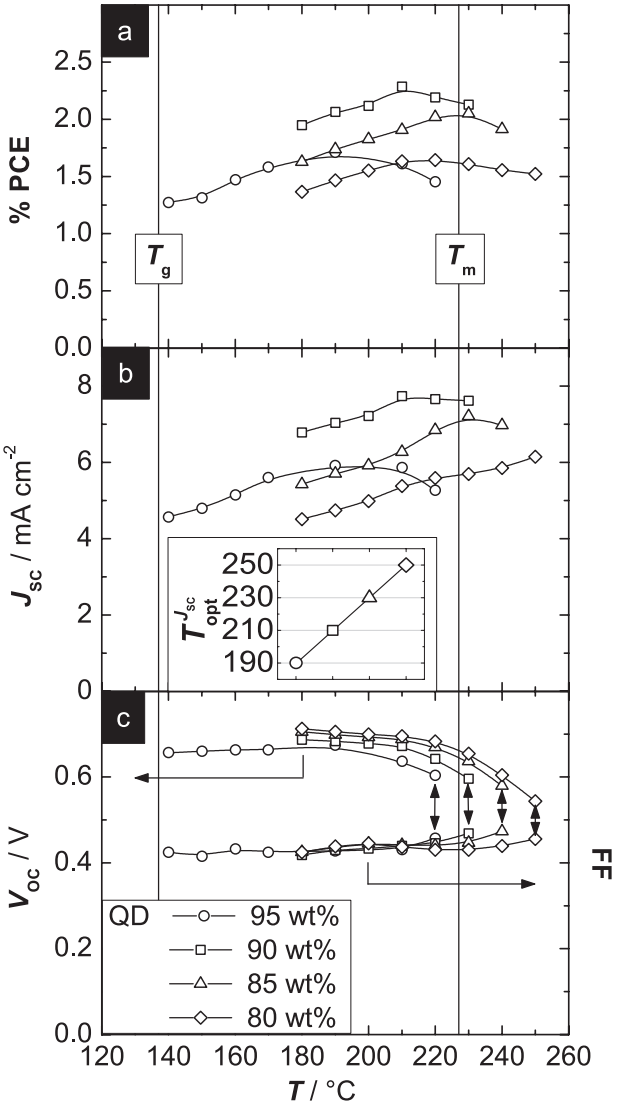


**Figure 2.** a) PCE, b) $J_{SC}$, and c) $V_{OC}$ and *FF* of solar cells made of different PCPDTBT/QD mass ratios plotted as a function of the annealing temperature. The inset in plot (b) presents the optimum annealing temperature giving the maximum $J_{SC}$ ($T_{opt}^{J_{SC}}$) for the QD loadings displayed in the legend of plot (c). The annealing time was 10 min for 5 wt% polymer and 20 min for all the other concentration ratios. The active layer thicknesses were $L \sim 76 \pm 3$ nm ($L_{opt} \sim 90$ nm). The glass transition temperature $T_g$ and the melting point $T_m$ of PCPDTBT are indicated in the plots by vertical lines. The lines are to guide the eye.

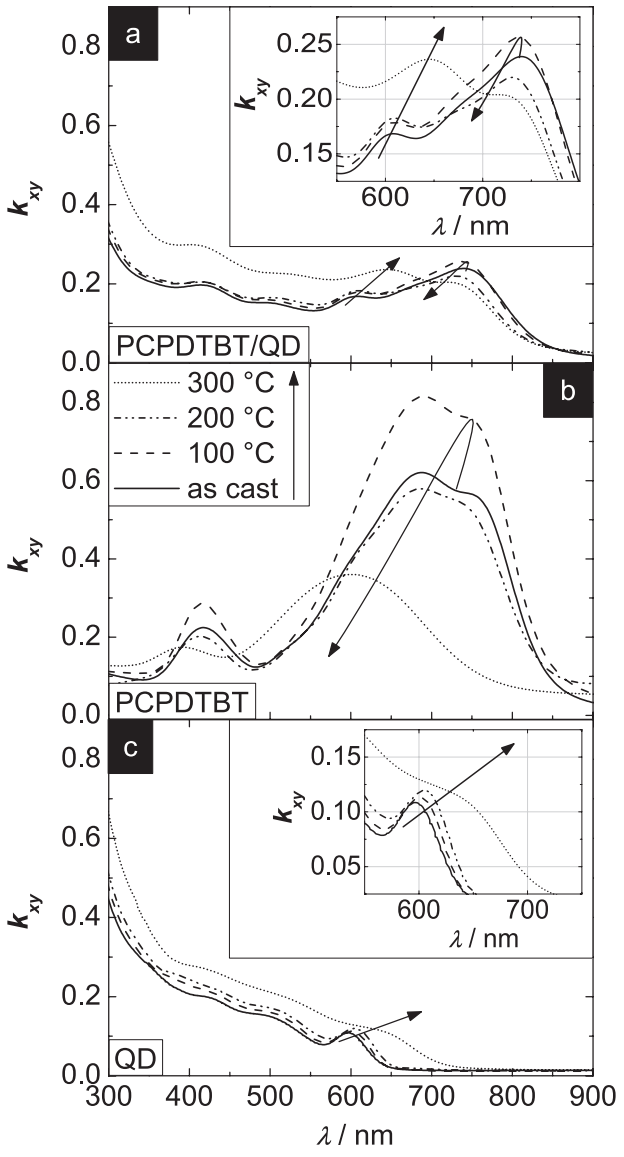


**Figure 3.** Extinction coefficients $k_{xy}$ in the plane of the film for different films spin-cast on ITO (125 nm) and PEDOT:PSS (55 nm) covered glass substrates for various annealing temperatures. a) PCPDTBT/QD = 10:90 wt%, b) neat PCPDTBT films, and c) neat QD films. The layer thickness was $L \sim 75 \pm 3$ nm for the blends, $L \sim 67 \pm 3$ nm for PCPDTBT films and $L \sim 81 \pm 5$ nm for the QD films. All films were annealed for 20 min at the temperature indicated in the plot.

increases with the temperature for all investigated polymer/QD loading ratios (Figure 2b), while $V_{OC}$ and *FF* remain essentially constant (Figure 2c). By contrast, at higher temperatures close to the melting point of the neat polymer ($T_m$ = 227 °C) $J_{SC}$ levels, while $V_{OC}$ and *FF* start to alter. Both effects together lead to an overall optimum annealing temperature to achieve the best device efficiency for a given QD loading (Figure 2a). The optimum temperature depends on the QD content, i.e., increases linearly with decreasing QD content (increasing PCPDTBT content) as displayed in the inset of Figure 2b (see also the Supporting Information, Figure S1).

To investigate the origin behind these observations, we considered the absorption of the films. **Figure 3** shows the extinction coefficients of the best blend films (10 wt% polymer) as well as the two individual components treated at different annealing temperatures. The data indicates that the absorption of PCPDTBT in both, neat film and mixture, first increases and slightly red-shifts (100 °C), becomes similar again (200 °C) to the as-cast film, and finally is strongly reduced and blue-shifted for elevated annealing temperature (300 °C). We attribute these findings to aggregation of the polymer chains upon annealing below the melting temperature $T_m$, as is commonly observed for many OPV polymers (among them P3HT[18]), while annealing above $T_m$ reduces aggregation leading to a more amorphous situation. For the QD, a slight red-shift of the absorption is observed in both, neat film and mixture, until 200 °C (from 597 nm in as cast films to 605 nm at 200 °C), while a strong red-shift and significant broadening is observed for annealing at 300 °C. We believe that this is due to sintering of the particles, which leads to an extended electronic system. This interpretation is supported by the fact that the series resistance ($R_S$) decreases with the annealing temperature, while the parallel resistance ($R_P$) slightly increases (**Figure 4**b). Both parameters correlate with *FF*.[19,21] Hence, an increasing FF with the annealing temperature results from a reduced interparticle resistance due to a better interconnectivity between the QD particles/domains.

In the higher temperature region, a changing $V_{OC}$ and *FF* play an important role for the overall performance. A $V_{OC}$ reduction with increasing annealing temperature[21] and $PC_{61}BM$ loading[22] has been reported for all organic PV. A lowering of $V_{OC}$ with increasing annealing temperature and QD loading was likewise observed in our devices. For 10 wt% PCPDTBT, $V_{OC}$ drops above 210 °C and displays an opposite trend relative to *FF* (Figure 2c). A general perception for all organic devices is that $V_{OC}$ is related to the energy difference between the HOMO of the donor and the LUMO of the acceptor.[24,25] Contact-potential differences (CPD) measured by Kelvin probe are an established way to evaluate the highest occupied states, i.e., HOMO or valence band (VB), of solid-state samples.[26,27]

Figure 4a shows the dependency of $V_{OC}$ on the CPD. A linear correlation between the two parametes is oberserved, the slope being 0.64. If only the donor phase was changing its electronic energy level upon annealing, a theoretical slope of unity would be expected. Since this is obviously not the case, we have to assume that in addition to the alteration of the donor phase the acceptor phase changes its electronic levels as well. As already discussed above, the observed red-shift of the QD absorption with increasing annealing temperatures indicates a change in the QD-interparticle interactions/agglomerates, leading to an alteration of the VB and CB of the QD owing to a reduced band gap ($E_g$) (Figure 3c). The $V_{OC}$ reduction comes along with a slight increase of *FF* with the annealing temperature and the QD loading for all D/A ratios. A higher QD content was found to extend the size of the agglomerated regions with an advanced QD connectivity,[27] in agreement with the increase in *FF*.

As most parameters in solar cell optimization influence each other, one should notice that each layer thickness *L* has an optimum concentration ratio of the donor and acceptor components, which balances the absorption and the charge

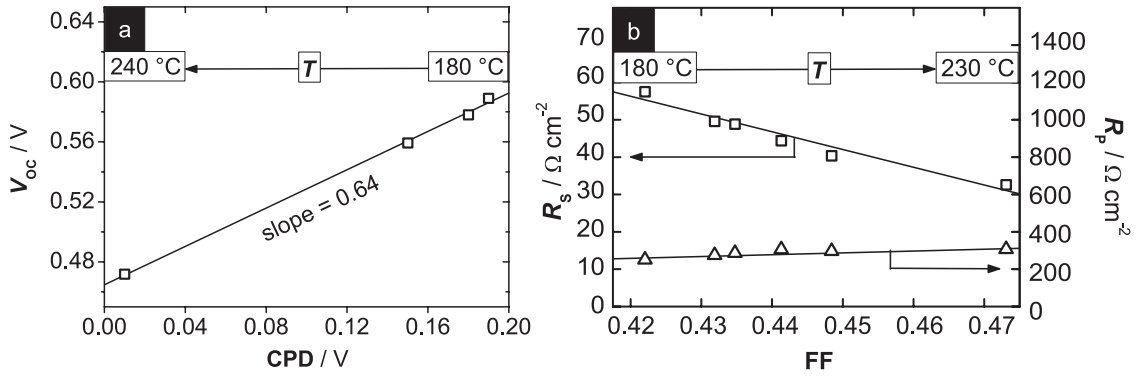


**Figure 4.** a) Correlation of the open-circuit voltage $V_{OC}$ and the contact potential difference CPD determined from thin films by Kelvin probe measurements with increasing annealing temperature $T$ for 180 °C, 200 °C, 220 °C, and 240 °C. The films consisted of PCPDTBT/QD blends with 90 wt% QD. The active layer thicknesses were $L \sim 72 \pm 3$ nm. The solid line presents the linear fit of the data. b) Correlation of the series resistance $R_S$ (squares, left axis) and parallel resistance $R_P$ (triangles, right axis) and the fill factor $FF$ under illumination with increasing annealing temperature $T$ from 180 °C to 230 °C in interval steps of 10 °C. The films consisted of PCPDTBT/QD blends with 90 wt% QD. The active layer thicknesses were $L \sim 76 \pm 3$nm. The solid lines present the linear fits to the data.

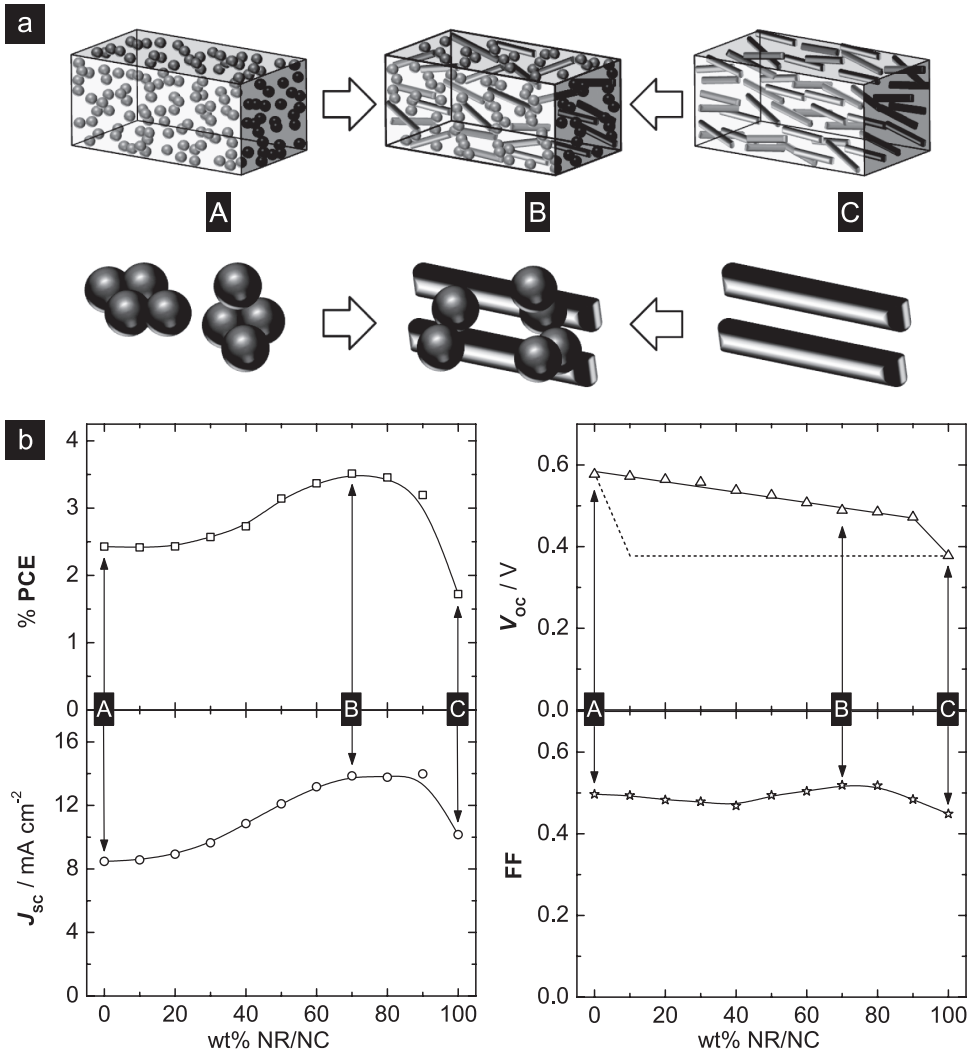


**Figure 5.** a) Schematic illustrations of NC in a polymer matrix. The QD/NR composite (B) forms the best interconnected pathway for electrons moving through the NC-network compared to QD (A) and NR (C) alone. b) PCE (squares), $J_{SC}$ (circles), $V_{OC}$ (triangles), and $FF$ (asterisks) of devices where the QD/NR weight ratio was varied while the polymer (PCPDTBT) content was kept constant at 10 wt%. The values for device A, B and C are labeled for further discussions. The films were annealed for 20 min at 210 °C and the active layer thickness was $L \sim 75 \pm 3$ nm. The lines are to guide the eye.

dissociation ratio.[28] The optimum active-layer thickness $L_{opt}$ for 10wt% PCPDTBT was found to be $L_{opt}$ ~ 90 nm, which resulted in a PCE of 2.8% ($J_{SC}$ = 8.94 mA cm$^{-2}$, $V_{OC}$ = 0.65 V, $FF$ = 0.48) for the best QD based cell (see the Supporting Information, Figure S2).

### 2.2. Blending PCPDTBT with Quantum Dots and Nanorods

In a recent study, electron tomography was used to investigate the film morphology of CdSe NC (*n*-butylamine as the capping ligand) blended with the polymer poly[2-methoxy-5-(3′,7′-dimethyloctyloxy)-1,4-phenylene vinylene] ($OC_1C_{10}$-PPV).[27] It was found that elongated nanorods in a polymer/NR blend film were oriented preferentially parallel to the plane of the film. Additionally, a previous report on the incorporation of colloidal CdSe QD into CdSe nanowire (NW) based photoelectrochemical devices (NW length ca. 1µm, no organic absorber)[29] argues that the transport connectivity within the network is improved to give a higher $J_{SC}$ resulting in a better device performance. These results suggest that the electron transport can be improved when the mostly parallel oriented NR could be linked by electronic interconnects such as the smaller spherical QD. Our basic idea of an improved nanoscale network is illustrated in **Figure 5**a.

To investigate and confirm this proposal, in a second step, different CdSe QD/NR ratios (pyridine as the capping ligand) were blended with PCPDTBT and processed under the same conditions as the best performing PCPDTBT/QD devices (90 wt% NC). The gradual exchange of spherical CdSe QD for rod-shaped CdSe NR with a length of approximately 20–30 nm as determined by transmission electrom microscopy (TEM) images (see Supporting Information, Figure S3) yielded a maximum device performance of PCE = 3.6%.

Figure 5b presents the electrical cell parameters of solar cells with different active-layer compositions. We observed an almost constant $FF$ and a linear decrease of $V_{OC}$ on the NR/NC ratio from $V_{OC}$ = 0.57 V for 100 wt% QD (device A) down to $V_{OC}$ = 0.37 V for 100 wt% NR (device C), indicative of energy level differences between QD and NR. At similar diameters, the exciton absorption peak of NR compared to QD is shifted to lower energies,[8] indicating a smaller band gap of the NR. We find that the relative absorption maximum of the NR (662 nm/1.87 eV) in annealed films (210 °C) is also located at a lower energy relative to the exciton absorption peak of the QD (618 nm/2.00 eV) (**Figure 6**b), which partially accounts for the $V_{OC}$ reduction of 0.2 V.

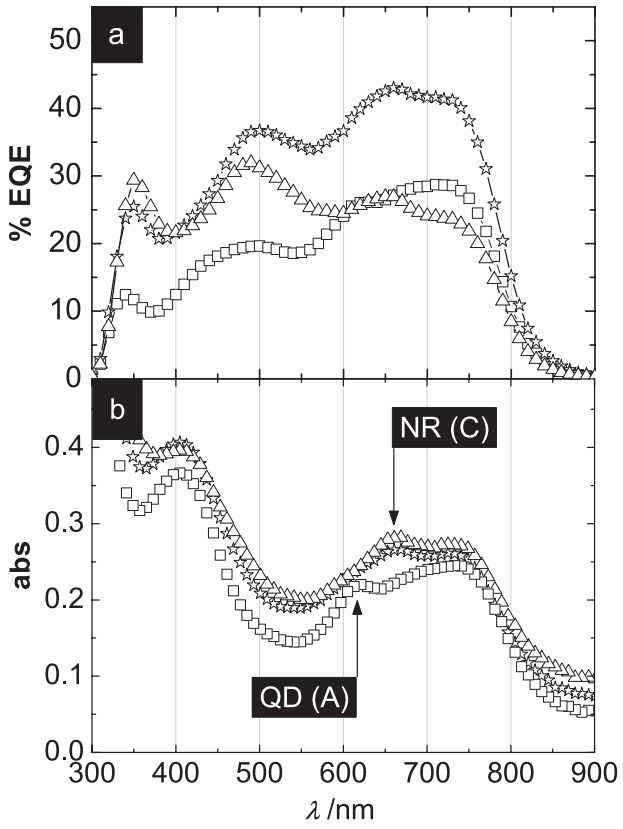


**Figure 6.** a) External quantum efficiency spectra and b) absorption spectra of devices A (squares), B (asterisks) and C (triangles) (see Table 1). The QD and NR exciton absorption bands are indicated in plot (b). All films were annealed for 20 min at 210 °C and had an equal layer thickness of $L$ ~ 75 ± 3 nm.

By contrast, a distinct optimum short-circuit current $J_{SC}$ of 13.86 mA cm$^{-2}$ was observed for the best operating device B (NR/NC = 0.66). UV–vis spectroscopy (Figure 6b) indicates a slightly increased absorption with increasing NR contents for films with identical layer thicknesses, supporting the assumption that the increase in $J_{SC}$ originates from a better connected n-type network and reduced recombination. This view is supported by scanning electron microscopy (SEM) images (**Figure 7**), which show a better fine structure for a medium NR content (B) to support the picture of an advanced NC-morphology/network. In comparison, device A shows a stronger phase separation between the polymer and the NC, while device

**Table 1.** Device performance parameters of PCPDTBT/QD/NR based solar cells with different component mass ratios. The films were annealed for 20 min at 210 °C and the active layer thickness was $L$ ~ 75 ± 3 nm.

| Blend Components [wt%] | | | | | | | PCE [%] | |
|---|---|---|---|---|---|---|---|---|
| Device | QD | NR | PCPDTBT | $J_{SC}$ [mA cm$^{-2}$] | $V_{OC}$ [V] | FF | Best | Average[a)] |
| A | 90 | 0 | 10 | 8.47 | 0.57 | 0.49 | 2.48 | 2.42 |
| B | 27 | 63 | 10 | 13.86 | 0.48 | 0.51 | 3.64 | 3.51 |
| C | 0 | 90 | 10 | 10.15 | 0.37 | 0.44 | 1.81 | 1.72 |

[a)]The parameters of PCEs were averaged over six solar cells.

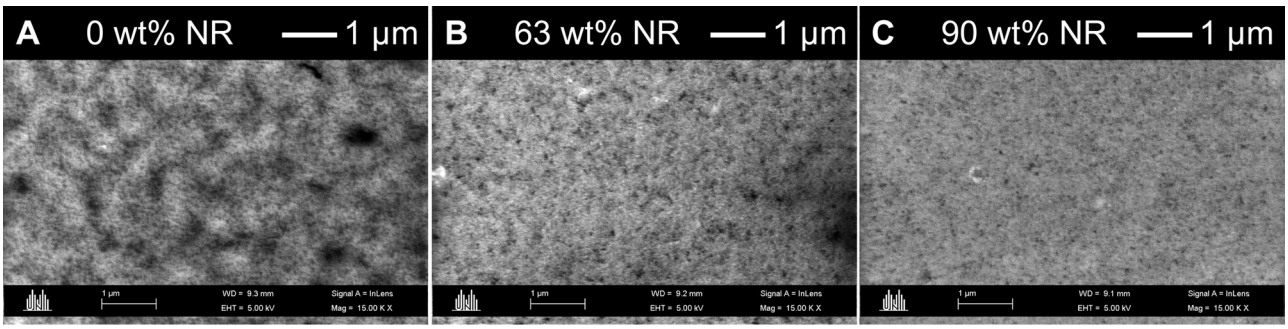


**Figure 7.** SEM images of PCPDTBT/NC blend films with different QD/NR ratios in the NC fraction (see Table 1). The films were annealed for 20 min at 210 °C. All films had an active layer thickness of $L \sim 75 \pm 3$ nm.

C provides the most homogeneous film surface regarding the material contrast.

Figure 6a presents the external quantum efficiencies (EQE) of the devices A, B and C. The gain in the electrical current for the QD/NR blend device B underlines the improved charge extraction at a comparable absorption. The maxima in the EQE plots at 500 nm and 700 nm confirm that light harvesting of the inorganic component significantly contributes to the charge generation and collection at the respective electrodes.

Numerous reports on polymer/NC blends characterize the phase separation of such composite films and the resulting total film morphology[28,32] owing to differences in solubility/dispersibility of the two material classes. By adding a second acceptor component with a different geometry, it is expected, that $V_{OC}$ is defined by the acceptor with the lower lying LUMO level (here the NR). This picture is outlined by the dotted curve in the $V_{OC}$ plot of Figure 5b. This clearly contradicts our experimental findings of a linear dependence for all QD/NR ratios except the single acceptor cell based on NR (device C). Alternatively, we propose a two-sub-phase system of the acceptor components (QD and NR), which would result in a working principle, where both NC shapes contribute to $V_{OC}$ as coexisting sub-cells.

Taking the QD/NR network into account, the proposed sub-phase separation of QD and NR is not precluding an advanced interconnection in the NC blend: It rather provides a compromise, where the two NC shapes partially form sub-agglomerates but still develop an electron-transporting network. The image of the interconnecting character of the QD is supported by the case of only NR in the acceptor phase (device C): a reduced connectivity due to the absence of small QD results in a strongly reduced $J_{SC}$.

## 3. Conclusions

In conclusion, two different PCPDTBT/CdSe NC hybrid systems are presented that afford an optimized power conversion efficiency of up to 2.8% for polymer/QD based cells and 3.6% for polymer/QD/NR active layer blends under simulated AM 1.5 illumination. The most important improvement in performance comes from the possibility of using a relatively high temperature for the thermal annealing step. For best performing devices a PCPDTBT:QD ratio of 10:90, forming a 90 nm thick active layer and an annealing temperature of 210 °C is found to be the optimum. In this regard, the QD-interconnectivity benefits from the high annealing temperature and transforms into an n-type structure where the particles form an extended network of agglomerates. This comes along with increased extinction coefficients and a lowered series resistance, which results in a higher short-circuit current. The applicable temperature is limited by a decrease of the open-circuit voltage, which is due to a lowering of the LUMO/VB energy level of the QD acceptor and a HOMO energy level increase of the PCPDTBT donor. Additionally, the device performance is reduced by a decrease in the absorption coefficient of PCPDTBT for higher annealing temperatures. Therefore, a polymer providing morphological and energetic stability at elevated temperatures could be an approach to overcome the trade-off between an advanced charge carrier percolation in the QD phase and a lowered optical absorption in the polymer phase.

As a second major finding, it turns out that an NR-network in combination with small spherical QD takes advantage of an improved connection between the mostly in plane aligned NR in the polymer matrix to further advance the electron-transport and to reduce recombination. This is in agreement with the electrical cell parameters, in particular an increase of the short-circuit current. The open-circuit voltage of the blend devices was shown to depend on the ratio of the two electron accepting NC shapes which suggests the ability of both structures to work independently in sub-phases, since both NC geometries contribute to the overall voltage. However, the gain in the short-circuit current for QD/NR blend devices indicates improved percolation pathways for electrons in the integrated NC phase.

## 4. Experimental Section

*Nanocrystal Syntheses*: Highly crystalline CdSe QD with a mean diameter of about 4.7 nm were synthesized by using a flow-through microreactor system comparable to a reported one[31] and a mixture of trioctylphosphine (TOP) and oleic acid (OA) ligands. NR were synthesized following a published procedure.[30] The nanoparticles were treated by methanol to remove excess synthesis ligands. Subsequently, they were stirred in n-hexane for at least 12 h to further remove the excess synthesis ligands and were washed afterwards twice with methanol. The washed nanoparticles were refluxed in pyridine at 108 °C for 8 h for ligand exchange.

*Sample Preparation*: All devices were fabricated on commercial indium-tin oxide (ITO)-coated glass. The ITO was etched with acid and

subsequently cleaned using chloroform, acetone, Mucasol detergent, and deionized water in an ultrasonic bath. Next, the ITO substrates were exposed to ozone for 15 min and immediately coated with poly(3,4-ethylenedioxythiophene)/poly(styrenesulfonate) (PEDOT:PSS, CLEVIOS HIL 1.3, Heraeus Clevios GmbH). Afterwards the samples were heat treated for 2 min at 110 °C to remove residual water. The photoactive BHJ layer was spin-cast from chlorobenzene in an $N_2$-filled glove box. PCPDTBT (PCPDTBT/QD blends: $M_n$ = 15.000 g mol$^{-1}$, $M_w$ = 23.000 g mol$^{-1}$ for PCPDTBT) (PCPDTBT/QD/NR blends: $M_n$ = 19.000 g mol$^{-1}$, $M_w$ = 26.000 g mol$^{-1}$ for PCPDTBT) was synthesized in Stille-type cross coupling polycondensations according to published procedures[32] and was solubilized at a proper concentration (15–20 mg mL$^{-1}$) in chlorobenzene. Before being incorporated into the polymer, QD- and NR-suspensions in pyridine were precipitated in pentane and suspended in chlorobenzene (60 mg mL$^{-1}$). The polymer solutions and the NC dispersions were prepared separately and combined prior to spincoating. The substrates were transferred to a high-vacuum chamber for evaporation of the metal contacts (consisting of 4 nm calcium covered by 150 nm silver) at a base pressure of $10^{-6}$–$10^{-7}$ mbar, both at deposition rates of about 0.3–2.0 Å s$^{-1}$ on top of the solution-processed BHJ-blends. The top-contact deposition was accomplished through a mask, leading to seven solar cells on each substrate with an active area of 0.08 cm$^2$.

*Device Characterization*: The *J–V* characteristics of the solar cells were measured using a Keithley 2425 source-measurement unit. The AM1.5 light was provided by a filtered Xe lamp. The intensity of 100 mW cm$^{-2}$ of the AM1.5 light was determined using a calibrated inorganic solar cell from the Fraunhofer Institute for Solar Energy (ISE - CalLab PV Cells) in Freiburg (Germany). No spectral mismatch factor was included in the calculation of the efficiency. A surface profiler (Dektak, Veeco) was used to determine the active layer thicknesses. UV–vis spectra were taken with a Varian Cary 50 spectrometer. EQE measurements were conducted with a setup from Newport Oriel Product Line using a 300 Watt Xenon, ozone free arc lamp and a Newport Cornerstone monochromator.

*SEM Images*: Measurements were performed in a NEON 40 from ZEISS (field-emission scanning electron microscope) at an acceleration voltage of 5.0 kV using an InLens-detector at a magnification of 15.000.

*Kelvin Probe Measurements*: The Kelvin probe system (Besocke Delta Phi GmbH) was installed in a self-designed chamber in argon atmosphere. Relative data of energy levels were obtained by measuring the contact potential difference (CPD) between the investigated polymer/NC blend films and a vibrating gold grid (diameter 2.5 mm) as reported before.[25] A set of materials with well known and constant work functions were used for calibration and to verify our results, e.g., palladium, chromium and aluminum with a native oxide layer.

*Determination of $R_S$ and $R_P$*: The series resistance $R_S$ under illumination was obtained as described in the literature[19] where it was calculated by a comparison of the *I–V* characteristics of PV devices in the dark and under illumination using the following equation:

$$R_S = \frac{V_{dark,mpp} - V_{light,mpp} - (|J_{SC}| - |J_{mpp}|)\,R_{S,dark}}{|J_{mpp}|} \quad (1)$$

where the index mpp is the maximum power point and the indices light and dark stand for characteristics taken under illumination and in the dark. $R_{S,\,dark}$ is the dark series resistance, which is given by:

$$R_{S,dark} = \frac{V_{dark,\,J_{SC}} - V_{OC}}{|J_{SC}|} \quad (2)$$

The parallel resistance $R_P$ under illumination was obtained by applying Ohm`s law, using the inverse slope of the linear fit between –0.1 V and 0.1 V in the *I–V* characteristics.

*Determination of $k_{xy}$*: The optical analysis was performed with an M2000 J.A.Woollam rotating compensator ellipsometer, using the wavelength range from 240–1700 nm and angles of incidence of 65°, 75°, and 85°. In addition the transmitted light intensity under normal angle of incidence was measured with the same tool, using different polarizations of the light. In order to reduce the impact of substrate back side reflection, this side was roughened and blackened previous to ellipsometric studies. The degree of depolarization was measured and used to identify sample non-idealities such as thickness inhomogeneity or extant back side reflection of the substrate material. Subsequently, mechanical step height profiles were measured with a Veeco Dektak150 at several positions along a scratch at the optical measurement position. The obtained values for the layer thickness were used as starting values and reference for the optical models.

The measured data were modelled with the software WVASE32 3.668, using the ellipsometric data ($\Psi$, $\Delta$) of the three angles of incidence and the transmitted light intensity combined in one model. Fit weighting was adjusted in order to equal the weight of transmission and ellipsometric data. The films of QD, NR, PCPDTBT and their blends were analyzed by coupled models of the experimental data on the substrates glass/PEDOT:PSS and glass/ITO/PEDOT:PSS. Both substrate systems were previously analyzed and kept constant during the film analysis. The applied analysis is based on the Kramers–Kronig (KK) consistent generalized oscillator model, using several Gaussian oscillators to represent the imaginary part ($\varepsilon_2$) of the dielectric function ($\varepsilon = \varepsilon_1 + i\varepsilon_2 = (n + ik)^2$). The real part ($\varepsilon_1$) is subsequently obtained by the KK-relation. The neat NC showed isotropic optical properties, while PCPDTBT and its blends showed uniaxial anisotropic behaviour, with main optical axis parallel to surface normal. Optical anisotropy is typical for conjugated polymers.[33–35] The sets of oscillators for the in-plane (*xy*) out-of-plane (*z*) component were modelled independently, leading to unique fit results. However, for normal angel of incidence only the *xy*-component of $\varepsilon$ has an impact on electromagnetic wave, and thus on the light harvest of the solar cell under standard conditions.

## Supporting Information

Supporting Information is available from the Wiley Online Library or from the author.

## Acknowledgements

We gratefully acknowledge financial support by the Federal Ministry of Education (BMBF) of Germany through the NanoPolySol project. We thank A. Joppich (University of Cologne) for taking the SEM images.

Received: August 4, 2011
Revised: October 5, 2011
Published online: November 17, 2011

[1] N. C. Greenham, X. Peng, A. P. Alivisatos, *Phys. Rev. B* **1996**, *54*, 17628.
[2] B. R. Saunders, M. L. Turner, *Adv. Colloid Interface Sci.* **2008**, *138*, 1.
[3] D. V. Talapin, J.-S. Lee, M. V. Kovalenko, E. V. Shevchenko, *Chem. Rev.* **2010**, *110*, 389.
[4] G. Yu, J. Gao, J. C. Hummelen, F. Wudl, A. J. Heeger, *Science* **1995**, *270*, 1789.
[5] A. P. Alivisatos, *Science* **1996**, *271*, 933.
[6] C. J. Brabec, F. Padinger, N. S. Sariciftci, *J. Appl. Phys.* **1999**, *85*, 6866.
[7] J. Yang, A. Tang, R. Zhou, J. Xue, *Sol. Energy Mater. Sol. Cells* **2011**, *95*, 476.
[8] S. Dayal, M. O. Reese, A. J. Fergusen, D. S. Ginley, G. Rumbles, N. Kopidakis, *Adv. Funct. Mater.* **2010**, *20*, 2629.
[9] Y. Zhou, F. S. Riehle, Y. Yuan, H.-F. Schleiermacher, M. Niggemann, G. A. Urban, M. Krüger, *Appl. Phys. Lett.* **2010**, *96*, 013304.
[10] B. Sun, N. C. Greenham, *Phys. Chem. Chem. Phys.* **2006**, *8*, 3557.

[11] B. Sun, H. J. Snaith, A. S. Dhoot, S. Westenhoff, N. C. Greenham, *J. Appl. Phys.* **2005**, *97*, 014914.
[12] I. Gur, N. A. Fromer, C.-P. Chen, A. G. Kanaras, A. P. Alivisatos, *Nano Lett.* **2007**, *7*, 409.
[13] S. Dayal, N. Kopidakis, D. C. Olson, D. S. Ginley, G. Rumbles, *Nano Lett.* **2010**, *10*, 239.
[14] C. Soci, I.-W. Hwang, D. Moses, Z. Zhu, D. Waller, R. Gaudiana, C. J. Brabec, A. J. Heeger, *Adv. Funct. Mater.* **2007**, *17*, 632.
[15] J. Hou, Z. Tan, Y. Yan, Y. He, C. Yang, Y. Li, *J. Am. Chem. Soc.* **2006**, *128*, 4911.
[16] D. Mühlbacher, M. Scharber, M. Morana, Z. Zhu, D. Waller, R. Gaudiana, C. Brabec, *Adv. Mater.* **2006**, *18*, 2884.
[17] C. Goh, R. J. Kline, M. D. McGehee, E. N. Kadnikova, J. M. J. Frechet, *Appl. Phys. Lett.* **2005**, *86*, 122110.
[18] L. Chang, H. W. A. Lademann, J.-B. Bonekamp, K. Meerholz, A. J. Moule, *Adv. Funct. Mater.* **2011**, *21*, 1779.
[19] D. Pysch, A. Mette, S. W. Glunz, *Sol. Energy Mater. Sol. Cells* **2007**, *91*, 1698.
[20] P. Schilinsky, C. Waldauf, J. Hauch, C. J. Brabec, *J. Appl. Phys.* **2004**, *95*, 2816.
[21] D. Chirvase, Z. Chiguvare, M. Knipper, J. Parisi, V. Dyakonov, J. C. Hummelen, *J. Appl. Phys.* **2003**, *93*, 3376.
[22] J. K. J. van Duren, X. Yang, J. Loos, C. W. T. Bulle-Lieuwma, A. B. Sieval, J. C. Hummelen, R. A. J. Janssen, *Adv. Funct. Mater.* **2004**, *14*, 425.
[23] V. D. Mihailetchi, P. W. M. Blom, J. C. Hummelen, M. T. Rispens, *J, Appl. Phys.* **2003**, *94*, 6849.
[24] K. Vandewal, K. Tvingstedt, A. Gadisa, O. Inganäs, J. V. Manca, *Nat. Mater.* **2009**, *8*, 904.
[25] N. M. Kronenberg, M. Deppisch, F. Würthner, H. W. A. Lademann, K. Deing, K. Meerholz, *Chem. Commun.* **2008**, *48*, 6489.
[26] F. Rossi, *Rev. Sci. Instrum.* **1992**, *63*, 4174.
[27] J. C. Hindson, Z. Saghi, J.-C. Hernandez-Garrido, P. A. Midgley, N. C. Greenham, *Nano Lett.* **2011**, *11*, 904.
[28] A. J. Moulé, J. B. Bonekamp, K. Meerholz, *J. Appl. Phys.* **2006**, *100*, 094503.
[29] Y. Yu, P. V. Kamat, M. Kuno, *Adv. Funct. Mater.* **2010**, *20*, 1464.
[30] J. Liu, T. Tanaka, K. Sivula, A. P. Alivisatos, J. M. J. Frechet, *J. Am. Chem. Soc.* **2004**, *126*, 6550.
[31] E. M. Chan, R. A. Mathies, A. P. Alivisatos, *Nano Lett.* **2003**, *3*, 199.
[32] Z. Zhu, D. Waller, R. Gaudiana, M. Morana, D. Mühlbacher, M. Scharber, C. J. Brabec, *Macromolecules* **2007**, *40*, 1981.
[33] U. Zhokhavets, G. Gobsch, H. Hoppe, N. S. Sariciftci, *Synth. Met.* **2004**, *143*, 113.
[34] L. A. A. Pettersson, S. Gosh, O. Inganäs, *Org. Electron.* **2002**, *3*, 143.
[35] A. J. Morfa, T. M. Barnes, A. J. Ferguson, D. H. Levi, G. Rumbles, K. L. Rowlen, J. van de Langemaat, *J. Polym. Sci., Part B: Polym. Phys.* **2011**, *49*, 186.